

Cluster Counting Algorithm for the CEPC Drift Chamber using LSTM and DGCNN*

Zhe-Fei Tian,¹ Guang Zhao,^{2,†} Ling-Hui Wu,² Zhen-Yu Zhang,^{1,‡} Xiang Zhou,¹
Shui-Ting Xin,² Shuai-Yi Liu,² Gang Li,² Ming-Yi Dong,^{2,3} and Sheng-Sen Sun^{2,3}

¹Hubei Nuclear Solid Physics Key Laboratory, School of Physics and Technology, Wuhan University, Wuhan 430072, China

²Institute of High Energy Physics, Chinese Academy of Sciences, Beijing 100049, China

³University of Chinese Academy of Sciences, Beijing 100049, China

Particle identification (PID) of hadrons plays a crucial role in particle physics experiments, especially for flavor physics and jet tagging. The cluster counting method, which measures the number of primary ionizations in gaseous detectors, represents a promising breakthrough in PID. However, developing an effective reconstruction algorithm for cluster counting remains a major challenge. In this study, we address this challenge by proposing a cluster counting algorithm based on long short-term memory and dynamic graph convolutional neural networks for the CEPC drift chamber. Leveraging Monte Carlo simulated samples, our machine learning-based algorithm surpasses traditional methods. Specifically, it achieves a remarkable 10% improvement in K/π separation for PID performance, which meets the necessary PID requirements for CEPC.

Keywords: Particle identification, Cluster counting, Machine learning, Drift chamber

I. INTRODUCTION

The Circular Electron Positron Collider (CEPC) [1, 2] is a large-scale collider facility proposed after the discovery of the Higgs boson in 2012. Designed with a circumference of 100 km and featuring two interaction points, the CEPC can operate at multiple center-of-mass energies. Specifically, it serves as a Higgs factory at 240 GeV [3–6], facilitates a W^+W^- threshold scan at 160 GeV, and functions as a Z factory at 91 GeV [7, 8]. Furthermore, it has the capability to be upgraded to 360 GeV for a $t\bar{t}$ threshold scan. Looking ahead, the CEPC can be further upgraded to a proton-proton collider, enabling direct exploration of new physics at a center-of-mass energy of approximately 100 TeV [9, 10]. The primary scientific objective of the CEPC is the precise measurement of the Higgs properties, particularly its coupling properties. Additionally, the trillions of $Z \rightarrow q\bar{q}$ events produced by the CEPC offer an excellent opportunity for studying flavor physics [11, 12].

Particle identification (PID) of hadrons is crucial in high energy physics experiments, especially for flavor physics and jet tagging [13]. Particle identification can help to suppress combinatorial backgrounds, distinguish between the same topology final-states, and provide valuable additional information for flavor tagging of jets. Future particle physics experiments such as CEPC require advanced detector techniques with PID performance that surpasses the current generation.

The drift chamber is one of the key detectors in high energy physics experiments. In addition to charged particle tracking, the drift chamber can also provide excellent PID while requiring almost no additional detector budget. For a drift chamber, PID is based on the ionization behavior of charged particles traversing the working gas. A well-established technique to identify particles is the average ionization energy loss per unit length (dE/dx) of charged particles measurement [14]. In a drift chamber cell, the charged particles ionize the gas, creating a cascade of electrons that can be detected as primary signals. This kind of ionization is called primary ionization, which is a Poisson process. Moreover, some of these electrons can also create secondary ionizations, leading to a Landau distributed dE/dx . The Landau distribution has an infinitely long tail and large fluctuations, which limits the dE/dx resolution [15]. Figure 1 shows an example of the waveform of the signal in a drift chamber cell.

Alternatively, the cluster counting technique directly measures the average number of primary ionizations per unit length in the waveforms processed by the fast electronics, rather than the dE/dx , which reduces the impact of the secondary ionizations [16] and significantly improves the PID performance. The resolution has the potential for a factor of 2 improvement for cluster counting. Therefore, the cluster counting technique, which is the most promising breakthrough in PID, is proposed for the future colliders for the high-energy frontier, such as the CEPC and the Future Circular Collider (FCC) [17]. A previous study of the cluster counting for the BESIII upgrade demonstrates that the cluster counting method has exhibited superior PID performance compared to the dE/dx method. It significantly enhanced the PID performance for π/K , achieving about 1.7 times the separation power of the dE/dx method [18].

Reconstruction is a significant challenge in cluster counting. An effective reconstruction algorithm must efficiently and accurately determine the number of primary ionizations in a waveform. However, the stochastic nature of ionization processes and the complexities of signals pose substantial obstacles in developing a reliable cluster counting algorithm. In traditional

* Supported by Joint Fund of Research utilizing Large-Scale Scientific Facility of the NSFC and CAS under Contract No. U2032114, National Natural Science Foundation of China (NSFC) under Contract No. 12275296, Institute of High Energy Physics (Chinese Academy of Sciences) Innovative Project on Sciences and Technologies under Contracts Nos. E3545BU210 and E25456U210.

† Corresponding author, zhaog@ihep.ac.cn

‡ Corresponding author, zhenyuzhang@whu.edu.cn

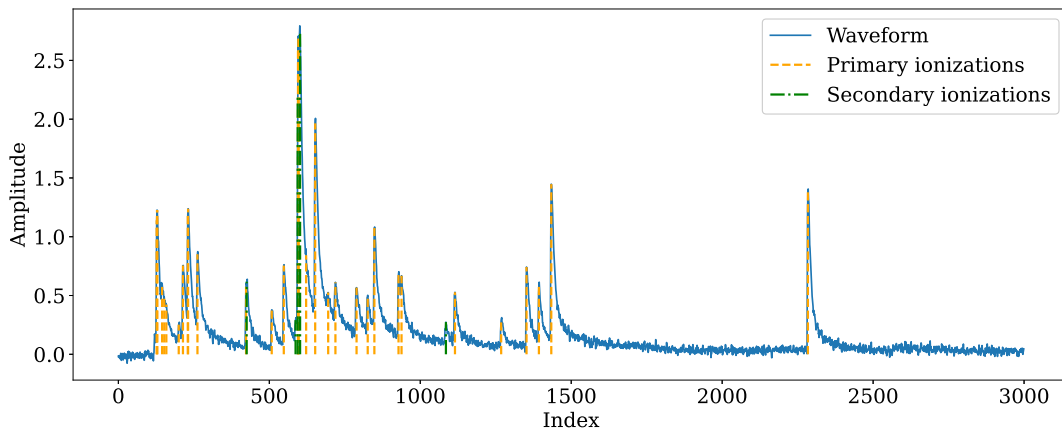


Fig. 1. A waveform example of induced current on a sense wire of a drift chamber. The x -axis represents the index of the waveform, which is sampled over a time window of 2000 ns at a sampling rate of 1.5 GHz. Both primary and secondary ionizations contribute to the waveform. The orange lines indicate peaks from primary ionizations. The green lines indicate peaks from secondary ionizations. An effective reconstruction algorithm needs to efficiently and accurately count the number of primary ionizations in the waveform.

methods, the cluster counting algorithm typically is decomposed into peak-finding (detect all peaks from both primary and secondary ionizations) and clusterization (determine the number of primary ionizations among the detected peaks in the previous step). For the derivative-based peak-finding, the first and second derivatives of the waveform are computed, and signals are detected by threshold crossing. Unfortunately, derivative-based algorithms struggle to achieve state-of-the-art performance, especially in scenarios with high pile-up and noise levels. For the time-based clusterization, as the average time differences between signals from different clusters tend to be larger than those within the same cluster, one can exploit this information to design peak-merging algorithms. However, due to significant overlap in the time difference distributions for the two cases (inter-cluster and intra-cluster), peak-merging algorithms often suffer from low accuracy.

Machine learning (ML) is a rapidly growing field of computer science that involves using of algorithms and statistical models to enable computer systems to improve their performance on a specific task by learning from data. Neural networks are the most commonly used ML technique at present, which is a set of computational models loosely inspired by the human brain consisting of an interconnected network. Recurrent neural networks (RNNs) [19] and graph neural networks (GNNs) [20] are both popular types of neural networks. In high energy physics, ML techniques are already being applied in many experiments, such as ParticleNet based on GNN [21] and its application on CEPC jet flavor tagging [22]. Machine learning has been preliminarily proved to be applicable in handling large-scale data in the field of high-energy physics. For cluster counting algorithm, ML can use the full information of the waveform and potentially uncover hidden features within the signal peaks. The problem can easily be modeled as a classification problem. Some mature ML tools can be applied, including PyTorch [23] and PyTorch Geometric [24].

In this paper, we present an ML-based algorithm for cluster counting that is optimized for the CEPC drift chamber. This paper proceeds as follows: Sec. II B introduces the fast simulation method and simulated samples used to train and test the ML-based algorithm. Sec. III introduces a new ML-based cluster counting algorithm. Sec. IV introduces the performance of the ML-based cluster counting algorithm and the comparison between it and traditional methods. Sec. V provides conclusions.

II. DETECTOR, SIMULATION AND DATA SETS

A. The CEPC Drift Chamber

In the design of the CEPC 4th conceptual detector, it is proposed to insert a drift chamber into the silicon inner tracker (SIT) and silicon external tracker (SET). This chamber primarily provides PID capability and can also enhance tracking and momentum measurement.

Based on the preliminary design, the length of the chamber is approximately 5800 mm, with a radial extent ranging from 600 mm to 1800 mm. The inner wall consists of a carbon fiber cylinder, while the outer support features a carbon fiber frame structure comprised of eight longitudinal hollow beams and eight rings. These components are covered with a gas envelope for sealing. The aluminum end plates are designed with a multi-stepped and tilted shape to minimize the deformation caused by wire tension. The schematic diagram of the drift chamber is shown in Fig. 2.

The entire chamber comprises approximately 67 layers. To meet the requirements for PID capability and momentum mea-

surement, the cell size of $18 \text{ mm} \times 18 \text{ mm}$ is adopted. Each cell consists of a sense wire surrounded by eight field wires, forming a square configuration. The sense wires are $20 \text{ }\mu\text{m}$ gold-plated tungsten wires, while the field wires are $80 \text{ }\mu\text{m}$ gold-plated aluminum wires. For achieving a suitable primary ionization density, a gas mixture of 90% He and 10% iC_4H_{10} is proposed.

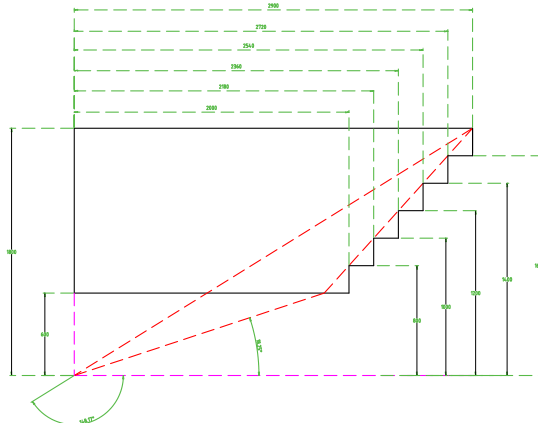


Fig. 2. Schematic layout of one-fourth of the CEPC drift chamber. The black lines show the boundaries of the drift chamber.

B. Simulation and Data Sets

For the cluster counting study, a sophisticated first-principle simulation package was developed. The package precisely simulates particle interactions and detector responses and creates realistic waveforms labeled with MC truth timing, which enables supervised training. The simulation package consists of two components: simulation and digitization. In the simulation, the geometry of drift chamber cells is constructed. Ionizations of charged particles are generated by the Heed package. To reduce computational expense, the transportation, amplification and signal creation processes for each electron are parameterized according to the Garfield++ simulation results, which outputs analog waveforms for drift chamber cells [25]. In the digitization, data-driven electronics responses and noise is considered. The impulse response of the preamplifier is measured from the experiment and further convoluted with the waveform. The noise is extracted from the experimental data using the fast Fourier transform and added to the signal using the inverse fast Fourier transform. The digitization outputs realistic digitized waveforms, which exhibit good agreement with experimental data in terms of rise time of the peak and noise level. The flowchart of simulation is shown in Fig. 3.

The geometry in the simulation package is based on the design of the CEPC 4th conceptual detector. According to the test beam experiments [26], the waveform roughly has a single-pulse rise time of 4 ns, a noise level of 5% and a sampling rate of 1.5 GHz. Based on the simulation package, MC samples with varying momenta are generated to train and test the neural networks algorithm. The detailed information of the samples is listed in Tab. 1.

Table 1. Summary of data sets used for training and testing ML-based cluster counting algorithms.

Purpose	Algorithm	Particle	Number of Events	Momentum (GeV/c)
Training	peak-finding	π^\pm	5×10^5	0.2 – 20.0
Testing	peak-finding	π^\pm	5×10^5	0.2 – 20.0
Training	Clusterization	π^\pm	5×10^5	0.2 – 20.0
Testing	Clusterization	π^\pm	$1 \times 10^5 \times 7$	5.0/7.5/10.0/12.5/15.0/17.5/20.0
Testing	Clusterization	K^\pm	$1 \times 10^5 \times 7$	5.0/7.5/10.0/12.5/15.0/17.5/20.0

III. METHODOLOGY

A. Algorithm Overview

An effective reconstruction algorithm for cluster counting must efficiently and accurately determine the number of primary ionizations in a waveform. As introduced in Sec. I, the cluster counting algorithm is usually decomposed into two steps:

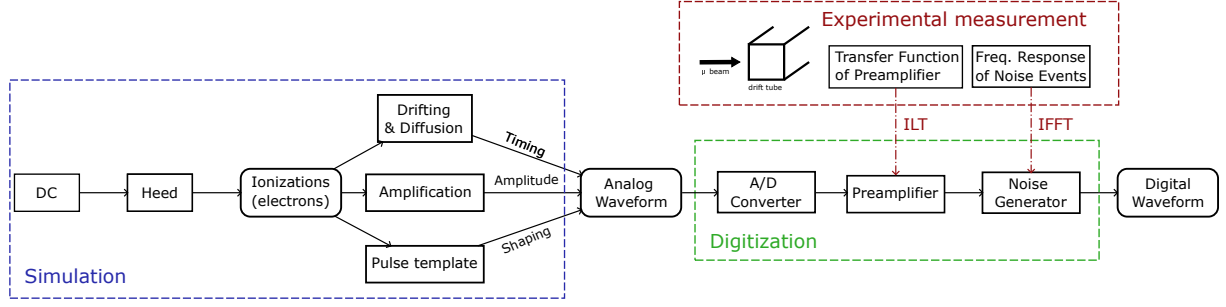


Fig. 3. Simulation package for cluster counting study. The package consists of simulation and digitization. The digitization takes input from the experimental measurement.

peak-finding and clusterization. The peak-finding detects peaks from both primary and secondary ionizations. While the clusterization discriminates primary ionizations from the peaks detected in the previous step.

The traditional peak-finding algorithm utilizes first and second derivatives on the waveform [27]. Ionization electron pulses, characterized by a swift rise (mere nanoseconds) and prolonged decay (tens of nanoseconds), yield pronounced derivative values, facilitating peak identification. Higher-order derivatives enhance hidden peak detection but increase noise susceptibility. To mitigate high noise levels, pre-processing with low-pass filters, such as moving averages, is recommended before applying derivatives. For clusterization, a peak-merging algorithm is employed. Electrons from a single primary cluster, typically localized spatially, exhibit proximate arrival times at the sensing wire, forming discernible clusters in the waveform. Timing information from peak detection aids in distinguishing primary from secondary electron signals. Nonetheless, due to potential overlap between electrons from distinct primary clusters, a precise peak-merging requirement is crucial for the clusterization algorithm.

The aforementioned traditional rule-based algorithms, which are dependent on incomplete raw hit information usage and human expertise, often fail to reach the state-of-the-art performance. In stark contrast, ML-based algorithms harness an abundance of labeled samples for supervised learning, adeptly extracting intricate data features. As for the cluster counting, in the first step, a long short-term memory (LSTM) network is employed to discriminate between signals and noise. Both primary and secondary ionization signals are detected in this step. The second step of the algorithm, clusterization, is achieved through a dynamic graph neural network (DGCNN). The DGCNN is used to further classify whether a detected peak in the first step is from primary ionization or not.

B. Peak-finding

The peak-finding algorithm is used to find all ionization peaks from a waveform. To reduce the complexity, the waveforms are divided into sliding windows with a window size of 15 data points. For each of these sliding windows, a label is added according to the MC truth information. The label can be either a signal candidate or a noise candidate, which defines the peak-finding as a binary classification.

To process the time series data in sliding windows, an LSTM-based network is explored for the peak-finding algorithm. The LSTM is a type of RNN that can process sequential data and has been successfully used in a range of applications [28]. RNNs are particularly effective for sequence modeling tasks, like sequence prediction and labeling, because they utilize a dynamic contextual window that captures the entire history of the sequence. However, RNNs exhibit limitations in effectively processing long sequences and are susceptible to issues related to vanishing and exploding gradients [29, 30].

The LSTMs have a unique architecture that includes memory blocks within the recurrent hidden layer. These memory blocks consist of memory cells and forget gates. The memory cells store the temporal state of the network through self-connections, while special multiplicative units known as gates regulate the information flow. Each memory block includes an input gate to manage input activations into the memory cell, an output gate to control the output flow of cell activations, and a forget gate to scale the internal state of the cell before adding it as input to the cell through self-recurrent connections, thereby adaptively forgetting or resetting the cell's memory [30, 31].

In this study, the neural network architecture of the LSTM-based peak-finding algorithm is summarized as follows:

- An LSTM layer

The LSTM layer is used for processing sequential data and capturing long-term dependencies between the data points. This LSTM layer has one feature in the input data and 32 features in the hidden state.

- Two linear layers

The neural network model consists of two linear layers that serve as fully connected layers. The first layer has an input size of 32 and an output size of 32. The second layer has an input size of 32 and an output size of 1. A sigmoid activation function [32] is applied to the output of the second layer to produce the final classification result.

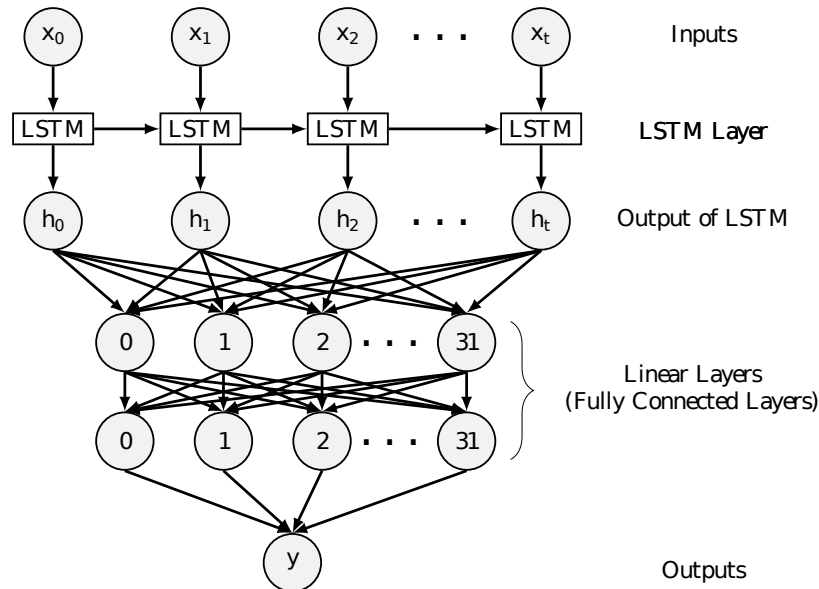


Fig. 4. The neural network structure of the LSTM-based model for the peak-finding algorithm.

Figure 4 shows the network structure of the LSTM-based model used to train the peak-finding algorithm. The model is trained on a simulated sample of π mesons. The sample includes 5×10^5 waveform events with momenta ranging from 0.2 GeV/ c to 20 GeV/ c . The data after preprocessing is divided into multiple batches, with each batch having a batch size of 64, and a total of 50 epochs for training.

The binary cross-entropy loss, a pivotal loss function for binary classification problems, quantifies the discrepancy between the true labels and the predicted probabilities, effectively guiding the model towards accurate predictions. This choice is driven by its effectiveness in handling cases where the output is a probability value between 0 and 1, making it particularly suited for our binary classification task. An Adam optimizer [33] is adopted with a learning rate of 10^{-4} , which is dropped by a factor of 0.5 every 10 epochs. To further enhance the algorithm performance, Optuna [34], a hyperparameter optimization framework, is used to tune the hyperparameters like learning rate and size of networks.

C. Clusterization

After performing the LSTM-based peak-finding algorithm, all the ionization signal peaks, including both primary and secondary ones, are detected. Therefore, the second algorithm, which is called clusterization algorithm, is developed to determine the number of primary ionization peaks.

In principle, secondary ionization occurs locally with respect to the primary electrons if the primary electrons have large enough energy. This leads to the electrons from a single cluster being located close to each other in the waveform. One can exploit this property to design an algorithm to discriminate between primary and secondary electrons. As mentioned in Sec. I, the traditional algorithm is developed based on the combination of adjacent peaks.

The GNN, which is operated on graph-structured data, can handle information with great complexity. The key design element of GNNs is the use of pairwise message passing, such that graph nodes iteratively update their representations by exchanging information with their neighbors [35]. For cluster counting, if the timing information of peaks is set as the node feature and the edges are initially connected according to timing similarities, GNNs can effectively learn the complex timing structure of the primary and secondary electrons through message passing.

The DGCNN is a special type of the GNN, which is applied to the clusterization algorithm. The DGCNN is designed to learn from the local structure of point clouds and can be used for high-level tasks such as classification and segmentation. The edge convolution layer, which is the essential component of DGCNNs, operates on graphs dynamically computed in each layer of the network. It is differentiable and can be plugged into existing architectures. In this work, the timings of the detected peaks in the peak-finding are represented as a graph. The timing of individual peaks is represented as the node feature. The

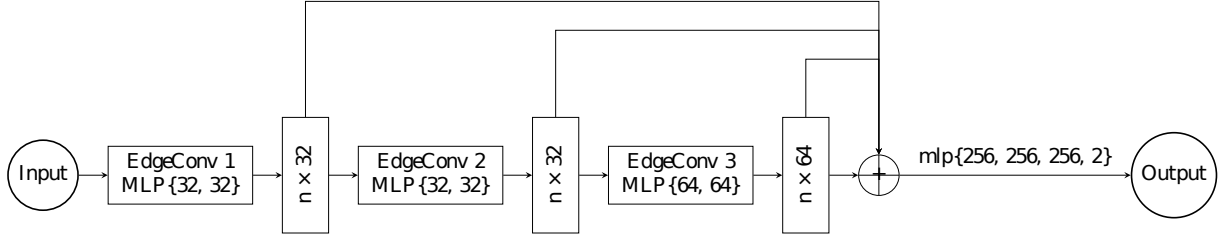


Fig. 5. The neural network structure of the DGCNN-based algorithm for clusterization.

edge distance is defined as the temporal similarity between nodes. The nodes are connected with the k^{th} nearest neighboring (k -NN) nodes [36]. During the training, with message passing, the nodes update their features and update the connections. Such a mechanism is expected to capture the hidden local relationships between peaks, thus achieving a better performance in classifying primary and secondary ionizations.

In this study, the neural network architecture of the clusterization algorithm is summarized as follows:

- Three dynamic edge convolution layers

Three dynamic edge convolution layers process graph-structured data by dynamically creating edges between each node and its neighboring nodes, thereby capturing local information. A new graph is generated at each layer of the GNN based on the k -NN approach [37]. The multi-layer perceptrons within the dynamic edge convolution layers map the number of input channels to the number of output channels. The features from three dynamic edge convolution layers were concatenated to get a $32 + 32 + 64 = 128$ dimensions output.

- A 4-layer multi-layer perceptron (MLP)

Multi-layer Perceptron (MLP) is a type of feedforward neural network that consists of multiple layers of neurons connected in a sequential manner [38]. This 4-layer MLP takes the concatenated output of the dynamic edge convolution layers as input. It has three hidden layers each with 256 neurons and 1 output layer with 2 channels. The dropout rate is set to 0.5, meaning that during training, each neuron in the network will have a 50% probability of being randomly dropped in order to prevent overfitting and encourage the network to learn more robust features. Finally, the model applies a log-softmax activation function to the output of the MLP and returns the classification probabilities.

Figure 5 shows the neural network architecture of the clusterization. The model is trained by a pion sample with 5×10^5 waveform events and momenta ranging from 0.2 GeV/c to 20 GeV/c. The data after preprocessing is divided into multiple batches, with each batch having a batch size of 128, and a total of 100 epochs for training.

For this binary classification model, the negative log-likelihood loss function and Adam optimizer are adopted with a learning rate of 10^{-3} , which is dropped by a factor of 0.5 every 10 epochs. All hyperparameters are tuned by Optuna, including the size of the three MLPs in dynamic edge convolution layers and the MLP that served as a fully connected layer. The value of k in k -NN, which determines how the dynamic edge convolution layers will establish the relationship between each node and its k nearest neighbors, is tuned to be 4.

IV. PERFORMANCE

The two-step model is trained using supervised learning on a large number of waveform samples. To evaluate the generalization performance of the model, it is applied on testing samples.

For peak-finding algorithm, both the LSTM-based algorithm and the traditional algorithm based on the second-derivative (D2) serve as classifiers. Their performance can be evaluated by the metrics of the classifier. In the context of classifiers, two commonly used metrics are precision and recall, which can also be referred to as purity and efficiency. The purity and efficiency are defined by true positive (TP), false positive (FP), and false negative (FN) [39], respectively. The specific definitions are provided in Eq. (1):

$$\begin{aligned} \text{Purity} &= \frac{\text{TP}}{\text{TP} + \text{FP}}, \\ \text{Efficiency} &= \frac{\text{TP}}{\text{TP} + \text{FN}}, \end{aligned} \quad (1)$$

where TP is the number of correctly detected peaks, (TP+FP) is the total number of detected peaks, and (TP+FN) is the total number of peaks in MC truth of the waveform. The LSTM-based peak-finding algorithm is tested on a π sample with momenta

ranging from 0.2 GeV/c to 20.0 GeV/c. The sample consists of 5×10^5 waveform events. For a classifier, the purity and efficiency values can be determined by applying varying probability thresholds. Figure 6 shows the purity and efficiency values of the LSTM-based peak-finding algorithm and the traditional D2 algorithm as a function of the threshold. For the LSTM-based algorithm, a threshold of 0.95 is set, which gives a purity of 0.8986 and an efficiency of 0.8820. For the D2 algorithm, the threshold is set to have a similar purity to the LSTM-based algorithm, which gives an efficiency of 0.6827 (Tab. 2). Therefore, the LSTM-based algorithm is more efficient than the D2 algorithm, especially for the pile-up recovery (as shown in Fig. 7).

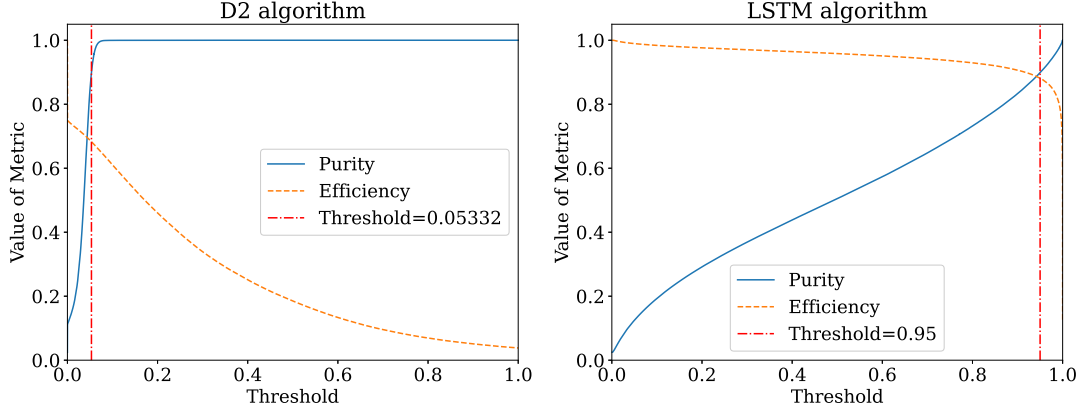


Fig. 6. Purity and efficiency as a function of the threshold for derivative-based D2 and LSTM-based algorithm, respectively. The blue solid line is the purity curve, the orange dashed line is the efficiency curve and the red dash dotted line is the optimized threshold. The threshold for the D2 algorithm acts on the second derivative. While the threshold for the LSTM algorithm applies to the predicted probability of the neural network, with a range of $[0,1]$. Any candidate that surpasses this threshold, either from D2 or LSTM algorithm, is considered as an ionization peak.

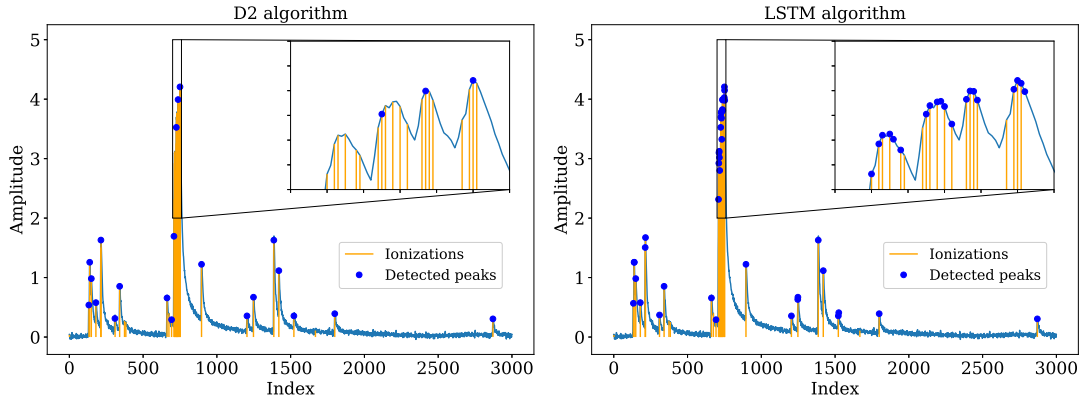


Fig. 7. Applying the derivative-based D2 and LSTM-based peak-finding algorithms on a simulated waveform. The x -axis represents the index of the waveform, which is sampled over a time window of 2000 ns at a sampling rate of 1.5 GHz. The blue points are the detected peaks. The orange lines are the peaks from the MC truth. The zoomed figure shows that the LSTM-based algorithm detects the pile-up peaks more accurately and more efficiently than the D2 algorithm.

Table 2. The purity and efficiency comparison between LSTM-based algorithm and traditional D2 algorithm for peak-finding.

	Purity	Efficiency
LSTM algorithm	0.8986	0.8820
D2 algorithm	0.8986	0.6827

The clusterization algorithm is applied after the peak-finding, aiming to determine the number of primary clusters from the detected peaks. After implementing both the LSTM-based peak-finding and DGCNN-based clusterization algorithms, one can obtain the number-of-cluster distribution of a charged particle and calculate the separation power for different kinds of charged particles. In our study, the clusterization is completed by performing node classification in DGCNN. To achieve the

best performance, threshold of the classifier is optimized by requiring the best K/π separation power. The K/π separation power is defined as

$$S = \frac{\left| \left(\frac{dN}{dx} \right)_{\pi} - \left(\frac{dN}{dx} \right)_{K} \right|}{(\sigma_{\pi} + \sigma_K)/2}, \quad (2)$$

where $dN/dx_{\pi(K)}$ and $\sigma_{\pi(K)}$ are the measured value and measured error of the number of primary ionizations per length for π (K). We perform the optimization using K/π samples with fixed momenta $p = 5.0$ GeV/ c , 7.5 GeV/ c , 10.0 GeV/ c , 12.5 GeV/ c , 15.0 GeV/ c , 17.5 GeV/ c , and 20.0 GeV/ c , respectively. The solid blue, dashed violet, and dashed cyan lines in Fig. 9 show the K/π separation power with different thresholds. According to the optimization, the model with a threshold of 0.26 achieves overall best performance.

With the optimized threshold, Fig. 8 presents a comparison of the number-of-cluster distributions between the MC truth, the traditional algorithm, and the DGCNN-based algorithm. It is evident that the mean value of the number-of-cluster distribution from the ML-based algorithm closely aligns with the MC truth, indicating that the ML-based algorithm achieves higher efficiencies than the traditional approach. Figure 9 illustrates the K/π separation powers from different algorithms at various momenta for 1 m track length. The ML cluster counting algorithm demonstrates approximately 10% better separation power across all momenta ranges compared to the traditional algorithms. Since the separation power scales with the square root of the track length, this performance improvement is roughly equivalent to having a detector with 20% larger radius coverage when using the traditional algorithm. Such an enhancement can significantly reduce the overall cost of the detector. Detailed numeric results are provided in Tab. 3. Additionally, we have extrapolated the K/π separation power from the 1 m track length to other track lengths. Figure 10 shows the K/π separation power for a 20 GeV/ c track as a function of the track length. Preliminary requirements for the CEPC include a 3σ K/π separation up to 20 GeV/ c momentum. Based on our PID performance obtained through the ML reconstruction algorithm, the current drift chamber design (radius within 600-1800 mm) meets the necessary PID requirements.

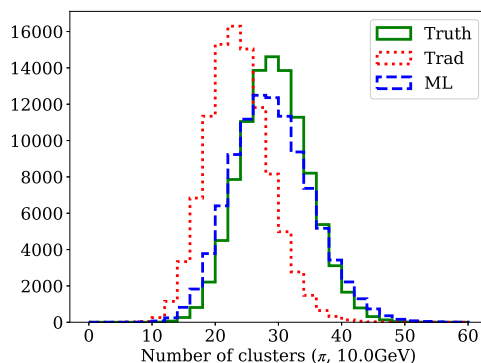


Fig. 8. The number-of-cluster distribution from MC truth (solid green), reconstruction by traditional algorithm (dotted red) and reconstruction by ML-based algorithm (dashed blue) for a 10 GeV/ c pion sample, respectively.

Table 3. Efficiency and separation power for charged K and π at various momenta and for different algorithms. The threshold of the ML-based algorithm is optimized as 0.95 for the LSTM-based peak-finding algorithm and 0.26 for the DGCNN-based clusterization algorithm. The efficiency is defined as the ratio of the number of reconstructed clusters to the number of MC truth clusters.

Algorithm	Metric	Momentum(GeV/ c)						
		5.0	7.5	10.0	12.5	15.0	17.5	20.0
ML-based algorithm	π^{\pm} efficiency	1.003	1.001	0.999	0.999	0.998	0.998	0.999
	K^{\pm} efficiency	1.014	1.011	1.010	1.008	1.006	1.004	1.003
	K/π separation power	4.203	4.279	4.081	3.832	3.509	3.216	2.921
Traditional algorithm	π^{\pm} efficiency	0.814	0.808	0.803	0.801	0.801	0.800	0.800
	K^{\pm} efficiency	0.837	0.830	0.824	0.820	0.817	0.814	0.812
	K/π separation power	3.888	3.954	3.765	3.550	3.277	3.054	2.697

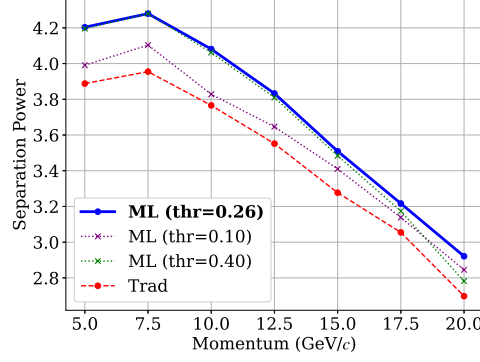


Fig. 9. The K/π separation power as a function of track momentum for 1 m track length. The red dashed line is from the traditional algorithm. The blue solid, violet dotted and green dotted lines are from the ML-based algorithm with a threshold of 0.26, 0.10 and 0.40, respectively. The blue solid line with a threshold of 0.26 achieves the overall best performance, which has a roughly 10% better K/π separation than the traditional algorithm.

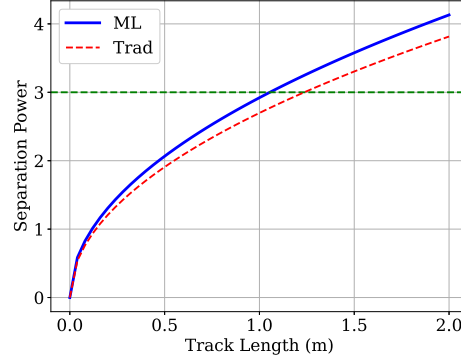


Fig. 10. The K/π separation power as a function of track length (L) at 20 GeV/ c . The curve is extrapolated from the value at $L = 1\text{m}$ by \sqrt{L} . The red dashed line is from the traditional algorithm. The blue solid line is from our ML-based algorithm with two steps. The green dashed line shows the target of 3σ separation power.

V. CONCLUSION

In this study, we have developed a cluster counting algorithm that incorporates both a peak-finding algorithm and a clusterization algorithm based on ML. Our approach offers several advantages over traditional methods for cluster counting. Specifically, our peak-finding algorithm demonstrates better efficiency compared to the derivative-based algorithm. The clusterization algorithm provides a Gaussian-distributed number of clusters and achieves an efficiency close to the ground truth (MC truth). The entire cluster counting algorithm outperforms the traditional methods, showcasing 10 % better K/π separation power. This level of PID performance with ML-based algorithms is roughly equivalent to having a 20% larger detector size with traditional algorithms. With such performance, the current design of the CEPC drift chamber meets the necessary PID requirements. Furthermore, the critical role of ML-based algorithms in cluster counting suggests their potential application in future high-energy physics experiments.

Data availability The data that support the findings of this study are openly available in Science Data Bank at <https://doi.org/10.57760/sciencedb.16322> and <https://cstr.cn/31253.11.sciencedb.16322>.

[1] The CEPC Study Group, CEPC Technical Design Report - Accelerator. (2023). doi: 10.48550/arXiv.2312.14363.

[2] The CEPC Study Group, CEPC conceptual design report: volume 2 - physics & detector. (2018). doi: 10.48550/arXiv.1811.10545.

- [3] F.F. An, Y. Bai, C.H. Chen et al., Precision Higgs physics at the CEPC. *Chin. Phys. C* **43**, 043002 (2019). doi: [10.1088/1674-1137/43/4/043002](https://doi.org/10.1088/1674-1137/43/4/043002).
- [4] D. Yu, M.Q. Ruan, V. Boudry et al., Higgs to $\tau\tau$ analysis in the future e^+e^- Higgs factories. (2019). doi: [10.48550/arXiv.1903.12327](https://doi.org/10.48550/arXiv.1903.12327).
- [5] Y. Bai, C.H. Chen, Y.Q. Fang et al., Measurements of decay branching fractions of $H \rightarrow b\bar{b}/c\bar{c}/g\bar{g}$ in associated $(e^+e^-/\mu^+\mu^-)H$ production at the CEPC. *Chin. Phys. C* **44**, 013001 (2020). doi: [10.1088/1674-1137/44/1/013001](https://doi.org/10.1088/1674-1137/44/1/013001).
- [6] Y.H. Tan, X. Shi, R. Kiuchi et al., Search for invisible decays of the Higgs boson produced at the CEPC. *Chin. Phys. C* **44**, 123001 (2020). doi: [10.1088/1674-1137/abb4d8](https://doi.org/10.1088/1674-1137/abb4d8).
- [7] P.X. Shen, P. Azzurri, C.X. Yu, M. Boonekamp et al., Data-taking strategy for the precise measurement of the W boson mass with a threshold scan at circular electron positron colliders. *Eur. Phys. J. B* **80**, 66 (2020). doi: [10.1140/epjc/s10052-019-7602-x](https://doi.org/10.1140/epjc/s10052-019-7602-x).
- [8] Z.J. Liang, Electroweak physics at CEPC. *Int. J. Mod. Phys. A* **34**, 1940013 (2019). doi: [10.1142/S0217751X1940013X](https://doi.org/10.1142/S0217751X1940013X).
- [9] J. Gao, CEPC-SPPC accelerator status towards CDR. *Int. J. Mod. Phys. A* **32**, 1746003 (2017). doi: [10.1142/S0217751X17460034](https://doi.org/10.1142/S0217751X17460034).
- [10] J. Gao, CEPC and SppC Status—From the completion of CDR towards TDR. *Int. J. Mod. Phys. A* **36**, 2142005 (2021). doi: [10.1142/S0217751X21420057](https://doi.org/10.1142/S0217751X21420057).
- [11] T.F. Zheng, J. Xu, L. Cao et al., Analysis of $B_c \rightarrow \tau\nu_\tau$ at CEPC. *Chin. Phys. C* **45**, 023001 (2021). doi: [10.1088/1674-1137/abcf1f](https://doi.org/10.1088/1674-1137/abcf1f).
- [12] L.F. Li, M.Q. Ruan, Y.D. Wang et al., Analysis of $B_s \rightarrow \phi\nu\bar{\nu}$ at CEPC. *Phys. Rev. D* **105**, 114036 (2022). doi: [10.1103/PhysRevD.105.114036](https://doi.org/10.1103/PhysRevD.105.114036).
- [13] Y.F. Zhu, S.Z. Chen, H.H. Cui et al., Requirement analysis for dE/dx measurement and PID performance at the CEPC baseline detector. *Nucl. Instrum. Meth. A* **1047**, 167835 (2023). doi: [10.1016/j.nima.2022.167835](https://doi.org/10.1016/j.nima.2022.167835).
- [14] G. Charpak, R. Bouclier, T. Bressani et al., The use of multiwire proportional counters to select and localize charged particles. *Nucl. Instr. and Meth.* **62**, 262-268 (1968). doi: [10.1016/0029-554X\(68\)90371-6](https://doi.org/10.1016/0029-554X(68)90371-6).
- [15] W. Blum, W. Riegler, L. Rolandi, Particle Detection with Drift Chambers. (2008). doi: [10.1007/978-3-540-76684-1](https://doi.org/10.1007/978-3-540-76684-1).
- [16] A. H. Walenta, The Time Expansion Chamber and Single Ionization Cluster Measurement. *IEEE Trans. Nucl. Sci.* **26**, 73-80 (1979). doi: [10.1109/TNS.1979.4329616](https://doi.org/10.1109/TNS.1979.4329616).
- [17] A. Abada, M. Abbrescia, S.S. AbdusSalam et al., FCC-ee: The Lepton Collider. *Eur. Phys. J. Spec. Top.* **228**, 261-623 (2019). doi: [10.1140/epjst/e2019-900045-4](https://doi.org/10.1140/epjst/e2019-900045-4).
- [18] S.T. Xin, G. Zhao, L.H. Wu et al., Simulation study of particle identification using cluster counting technique for the BESIII drift chamber. *J. Instrum.* **18**, T01006 (2023). doi: [10.1088/1748-0221/18/01/T01006](https://doi.org/10.1088/1748-0221/18/01/T01006).
- [19] A. Sherstinsky, Fundamentals of recurrent neural network (RNN) and long short-term Memory (LSTM) network. *Phys. D: Nonlinear Phenom.* **404**, 132306 (2020). doi: [10.1016/j.physd.2019.132306](https://doi.org/10.1016/j.physd.2019.132306).
- [20] J. Zhou, G. Cui, S.D. Hu et al., Graph neural networks: A review of methods and applications. *AI Open* **1**, 57-81 (2020). doi: [10.1016/j.aiopen.2021.01.001](https://doi.org/10.1016/j.aiopen.2021.01.001).
- [21] H.L. Qu, L. Gouskos, Jet tagging via particle clouds. *Phys. Rev. D* **101**, 056019 (2020). doi: [10.1103/PhysRevD.101.056019](https://doi.org/10.1103/PhysRevD.101.056019).
- [22] Y.F. Zhu, H. Liang, Y.X. Wang et al., ParticleNet and its application on CEPC jet flavor tagging. *Eur. Phys. J. C* **84**, 152 (2024). doi: [10.1140/epjc/s10052-024-12475-5](https://doi.org/10.1140/epjc/s10052-024-12475-5).
- [23] A. Paszke, S. Gross, F. Massa et al., PyTorch: An Imperative Style, High-Performance Deep Learning Library. *Adv. Neural Inf. Process Syst.* **32**, 8024-8035 (2019). doi: [10.48550/arXiv.1912.01703](https://doi.org/10.48550/arXiv.1912.01703).
- [24] M. Fey, J.E. Lenssen, Fast graph representation learning with PyTorch Geometric. *ICLR Workshop on Representation Learning on Graphs and Manifolds* (2019). doi: [10.48550/arXiv.1903.02428](https://doi.org/10.48550/arXiv.1903.02428).
- [25] D. Pfeiffer, L. De Keukeleere, C. Azevedo et al., Interfacing Geant4, Garfield++ and Degrad for the simulation of gaseous detectors. *Nucl. Instr. and Meth. A* **935**, 121-134 (2019). doi: [10.1016/j.nima.2019.04.110](https://doi.org/10.1016/j.nima.2019.04.110).
- [26] C. Caputo, G. Chiarello, A. Corvaglia et al., Particle identification with the cluster counting technique for the IDEA drift chamber. *Nucl. Instr. and Meth. A* **1048**, 167969 (2023). doi: [10.1016/j.nima.2022.167969](https://doi.org/10.1016/j.nima.2022.167969).
- [27] G. Zhao, L.H. Wu, F. Grancagnolo et al., Peak finding algorithm for cluster counting with domain adaptation. *Comput. Phys. Commun.* **300**, 109208 (2024). doi: [10.1016/j.cpc.2024.109208](https://doi.org/10.1016/j.cpc.2024.109208).
- [28] S. Hochreiter, J. Schmidhuber, Long short-term memory. *Neural Comput.* **9**, 1735-1780 (1997). doi: [10.1162/neco.1997.9.8.1735](https://doi.org/10.1162/neco.1997.9.8.1735).
- [29] Y. Bengio, P. Simard, P. Frasconi, Learning long-term dependencies with gradient descent is difficult. *IEEE Trans. Neural Netw.* **5**, 157-166 (1994). doi: [10.1109/72.279181](https://doi.org/10.1109/72.279181).
- [30] Y. Yu, X.S. Si, C.H. Hu et al., A review of recurrent neural networks: LSTM cells and network architectures, *Neural Comput.* **31**, 1235-1270 (2019). doi: [10.1162/neco_a_01199](https://doi.org/10.1162/neco_a_01199).
- [31] F.A. Gers, J. Schmidhuber, F. Cummins, Learning to forget: Continual prediction with LSTM, *Neural Comput.* **12**, 2451-2471 (2000). doi: [10.1162/089976600300015015](https://doi.org/10.1162/089976600300015015).
- [32] J. Han, C. Moraga, The influence of the sigmoid function parameters on the speed of backpropagation learning. *From Natural to Artificial Neural Computation* (1995). doi: [10.1007/3-540-59497-3_175](https://doi.org/10.1007/3-540-59497-3_175).
- [33] D.P. Kingma, J. Ba, Adam: A method for stochastic optimization. *Proceedings of the 3rd International Conference on Learning Representations* (2015). doi: [10.48550/arXiv.1412.6980](https://doi.org/10.48550/arXiv.1412.6980).
- [34] T. Akiba, S. Sano, T. Yanase et al., Optuna: A Next-generation Hyperparameter Optimization Framework. *Proceedings of the 25th ACM SIGKDD International Conference on Knowledge Discovery & Data Mining*, 2623-2631 (2019). doi: [10.48550/arXiv.1907.10902](https://doi.org/10.48550/arXiv.1907.10902).
- [35] J. Gilmer, S.S. Schoenholz, P.F. Riley, et al., Neural message passing for quantum chemistry, *Proceedings of the 34th International Conference on Machine Learning* **70**, 1263-1272 (2017). doi: [10.48550/arXiv.1704.01212](https://doi.org/10.48550/arXiv.1704.01212).
- [36] Y. Wang, Y.B. Sun, Z.W. Liu et al., Dynamic graph CNN for learning on point clouds. *ACM Trans. Graph.* **38** (2019). doi: [10.1145/3326362](https://doi.org/10.1145/3326362).
- [37] Z.H. Zhang, Introduction to machine learning: k-nearest neighbors. *Ann. Transl. Med.* **4** (2016). doi: [10.21037/atm.2016.03.37](https://doi.org/10.21037/atm.2016.03.37).
- [38] A. Pinkus et al., Approximation theory of the MLP model in neural networks. *Acta Numer.* **8**, 143-195 (1999).

doi: [10.1017/S0962492900002919](https://doi.org/10.1017/S0962492900002919).

- [39] M. Hossin, M. N. Sulaiman, A review on evaluation metrics for data classification evaluations. *Int. J. Data Min. Knowl. Manag. Process* **5**, 1 (2015). doi: [10.5121/ijdkp.2015.5201](https://doi.org/10.5121/ijdkp.2015.5201).